ELSEVIER

Three-dimensional probabilistic anatomical cranio-cerebral correlation via the international 10–20 system oriented for transcranial functional brain mapping

Masako Okamoto,[a,1] Haruka Dan,[a,1] Kuniko Sakamoto,[a] Kazuhiro Takeo,[b] Koji Shimizu,[b] Satoru Kohno,[b] Ichiro Oda,[c] Seiichiro Isobe,[a] Tateo Suzuki,[a] Kaoru Kohyama,[a] and Ippeita Dan[a,*]

[a] National Food Research Institute, Tsukuba 305-8642, Japan
[b] Medical Systems Division, Shimadzu Corporation, Kyoto 604-8511, Japan
[c] Technology Research Laboratory, Shimadzu Corporation, Kyoto 619-0237, Japan

The recent advent of multichannel near-infrared spectroscopy (NIRS) has expanded its technical potential for human brain mapping. However, NIRS measurement has a technical drawback in that it measures cortical activities from the head surface without anatomical information of the object to be measured. This problem is also found in transcranial magnetic stimulation (TMS) that transcranially activates or inactivates the cortical surface. To overcome this drawback, we examined cranio-cerebral correlation using magnetic resonance imaging (MRI) via the guidance of the international 10–20 system for electrode placement, which had originally been developed for electroencephalography. We projected the 10–20 standard cranial positions over the cerebral cortical surface. After examining the cranio-cerebral correspondence for 17 healthy adults, we normalized the 10–20 cortical projection points of the subjects to the standard Montreal Neurological Institute (MNI) and Talairach stereotactic coordinates and obtained their probabilistic distributions. We also expressed the anatomical structures for the 10–20 cortical projection points probabilistically. Next, we examined the distance between the cortical surface and the head surface along the scalp and created a cortical surface depth map. We found that the locations of 10–20 cortical projection points in the standard MNI or Talairach space could be estimated with an average standard deviation of 8 mm. This study provided an initial step toward establishing a three-dimensional probabilistic anatomical platform that enables intra- and intermodal comparisons of NIRS and TMS brain imaging data.

Keywords: Probabilistic anatomical platform; Transcranial magnetic stimulation; Human brain mapping; Near-infrared spectroscopy

* Corresponding author. National Food Research Institute, 2-1-12 Kannondai, Tsukuba 305-8642, Japan. Fax: +81-29-838-8122.

E-mail address: dan@nfri.affrc.go.jp (I. Dan).

[1] These two authors contributed equally to this work.

Available online on ScienceDirect (www.sciencedirect.com.)

Introduction

Near-infrared spectroscopy (NIRS) is an optical method that noninvasively monitors cerebral hemodynamics by measuring changes in the attenuation of near-infrared light passing through tissue. NIRS has proven to be effective in assessing oxygenation changes in response to functional brain activation in many studies, utilizing the tight coupling between neural activity and regional cerebral blood flow (Villringer and Chance, 1997; Villringer and Dirnafl, 1995). In contrast to other functional brain imaging methods such as functional magnetic resonance imaging (fMRI) or positron emission tomography (PET), NIRS requires only compact experimental systems, is less restrictive, and is relatively robust to body movement. Owing to these features, NIRS provides researchers with a high capacity to test a wide variety of experimental paradigms and the flexibility for long-term and repetitive monitoring. The recent advent of a multichannel version of NIRS has expanded its technical potential for human brain mapping (Hoshi et al., 2000; Isobe et al., 2001; Miyai et al., 2001; Takahashi et al., 2000; Watanabe et al., 1996, 1998). However, there is a technical drawback intrinsic to NIRS in that it measures cortical activities from the head surface without anatomical information of the brain to be examined.

Another newly developing noninvasive functional brain mapping technique, transcranial magnetic stimulation (TMS), also suffers from this technical drawback (Barker et al., 1985; Curra et al., 2002; Terao and Ugawa, 2002). TMS applies magnetic stimuli from a certain point on the head surface on the underlying cortical target to affect cortical neuronal activity. However, structural information for the cortical target is not available when TMS is used alone.

One commonly used solution is to examine cranio-cerebral structural correspondence in all subjects or a subset of the subjects using MRI to find the cortical structure underlying a given set of NIRS channels or TMS set points. However, such measurement is troublesome, requires expensive facilities, and thus diminishes the usefulness of NIRS and TMS measurement. A more desirable
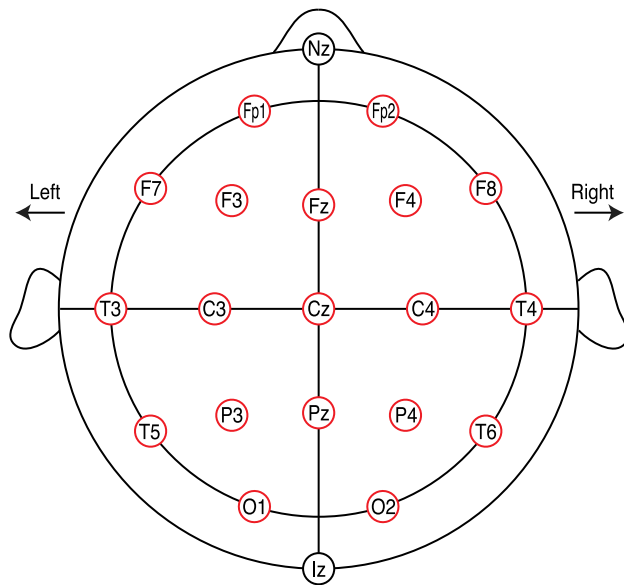
Fig. 1. Names and positions of the international 10–20 system used in this study. Nineteen standard positions in the conventional 10–20 system are shown (red circles). Nasion and inion are indicated as Nz and Iz.

solution would be to provide pre-examined cranio-cerebral structural correlation data as a common platform available for all researchers. The following should be satisfied for such a platform. First, the common platform should be optimized for transcranial brain mapping methods so that each researcher can examine transcranial brain mapping data using that modality alone. Second, the common platform should be presented in a standardized form that enables data comparison with other brain-imaging modalities. Third, it should have an expandable format for future applications.

Currently, the best way to assess the cranio-cerebral structural correlation is to utilize the international 10–20 system of electrode placement that serves as the recognized standard for scalp electrode positioning for electroencephalography (EEG) (Jasper, 1958). The system utilizes measurements of external landmarks on the scalp to determine relative cranial positions on the head surface of a subject (Fig. 1). A basic assumption of the system is that there is a consistent correlation between scalp locations and their underlying cerebral structures. Several studies have examined the validity of the structural correlation using cadavers (Blume et al., 1974; Jasper, 1958), X-ray (Morris et al., 1986), CT scans (Homan et al., 1987;

Myslobodsky and Bar-Ziv, 1989; Myslobodsky et al., 1990), and MRI (Gevins and Illes, 1991; Jack et al., 1990; Lagerlund et al., 1993; Steinmetz et al., 1989; Towle et al., 1993; Van den Elsen and Viergever, 1991).

There are two important factors in establishing the standard for cranio-cerebral structural correlation: its correspondence to a standard coordinate and its anatomical description. These two factors should be expressed probabilistically. In these respects, Homan et al. (1987) presented a pioneering work where they plotted the 10–20 standard positions on the Brodmann's cortical map from the temporal view and successfully described cranio-cerebral structural correlations on the Brodmann's plane, the standard cortical coordinates at that time (Brodmann, 1909, 1912). Moreover, they estimated the cortical structure corresponding to the 10–20 standard positions utilizing Brodmann's cortical map. Although providing intuitive histological appreciation, their work lacked statistical description and their methods could not circumvent a marginal–central resolution gap brought about by dimensional conversion from space to plane. Towle et al. (1993) and Lagerlund et al. (1993) gave effective solutions to these problems. They fit cranial and cerebral surfaces to a sphere and described the cortical positions that underlie the 10–20 electrode (cortical projection points) in three-dimensional coordinates. However, these efforts could not provide a fine histological description of the 10–20 cortical projection points in spatial coordinates as given for the planar one by Homan et al. (1987). After these studies, the main interest of EEG studies diverged from finding correspondence between the 10–20 standard positions and cortical surface structures to three-dimensional signal source detection. However, the former information is important for NIRS and TMS measurements. Thus, cranio-cerebral standardization in three-dimensional coordinates and its anatomical description supplemented with statistical treatment have been anticipated for transcranial brain-mapping studies.

One solution is to normalize gross brain structures to a standard template such as the Montreal Neurological Institute (MNI) and Talairach brains routinely used for fMRI and PET studies (Brett et al., 2002). If the 10–20 standard positions were adequately cast on the underlying cerebral surface in a standard brain, they could be normalized and expressed in standard stereotactic coordinates. After normalization, the 10–20 cortical projection point positions can be integrated across individuals, statistically treated and compared to the locations in the Talairach atlas (Talairach and Tournoux, 1988). Therefore, in this report, we examine the stereotactic cranio-cerebral correlation by determining the 10–20 cortical projection points in 17 healthy subjects, normalizing them to the

Fig. 2. Explanations for methods used in this research. (A) Fixation of a fatty marker on a hairy head surface. (B) Head surface image including markers in a three-dimensional view. Convexes are fatty markers placed on the 10–20 standard positions. Some additional positions are also visible. (C) Gradient sphere drawn by the DrawMSphere program. (D) Conceptual image to depict the overlay of a gradient sphere on a coronal section of an MR image. (E) Gradient sphere overlaid on a brain surface in a three-dimensional view. (F) Determination of the cortical projection point (red dot) when the closest point on the cortical surface (blue dot) from a 10–20 standard position on the head surface (purple dot) is a single point. Purple and blue lines represent head and cortical surfaces. A red circle represents a distance from a 10–20 standard position. An example of such a case is shown on the right shoulder. (G) Determination of the cortical projection point (red dot) when the minimum-distance points on the cortical surface (blue dot) from a 10–20 standard position on the head surface (purple dot) are two points at the same distance. Purple and blue lines represent head and cortical surfaces. A red circle represents a distance from a 10–20 standard position. An example of such a case is shown on the right shoulder. (H) Determination of the cortical projection point (red dot) when the minimum-distance points on the cortical surface (blue dot) from a 10–20 standard position on the head surface (purple dot) are two points at different distances. An example of such a case is shown on the right shoulder. Purple and blue lines represent head and cortical surfaces. Red circles represent distances from a 10–20 standard position. (I) Determination of the cortical projection point (red dot) when the minimum-distance points on the cortical surface (blue dot) from a 10–20 standard position on the head surface (purple dot) are three points at different distances. A purple line represents head surface. Gray convexes represent cortical surface. A green line represents a perpendicular line to a place defined by three points on cortical surface (pink triangle). An example of such a case is shown on the right shoulder. (J) Distance distribution from the cortical surface expressed as a gradient.

MNI brain, describing their locations in the MNI and Talairach coordinates with statistical considerations, and estimating their anatomical features. Furthermore, since NIRS and TMS measurements are sensitive to the depth of the cortical surface from the head surface, we examined the depth along the head surface and created a cortical surface depth map. In doing so, we hope to present a three-dimensional anatomical platform that facilitates intra- and inter-modal comparisons of transcranial brain imaging data.

Methods

Subjects

Seventeen healthy volunteers (Mongoloids; 9 males, 8 females; aged 22–51 years) participated in this study with informed consent. Fourteen were right-handed and 3 were left-handed. They did not have any neurological abnormalities.
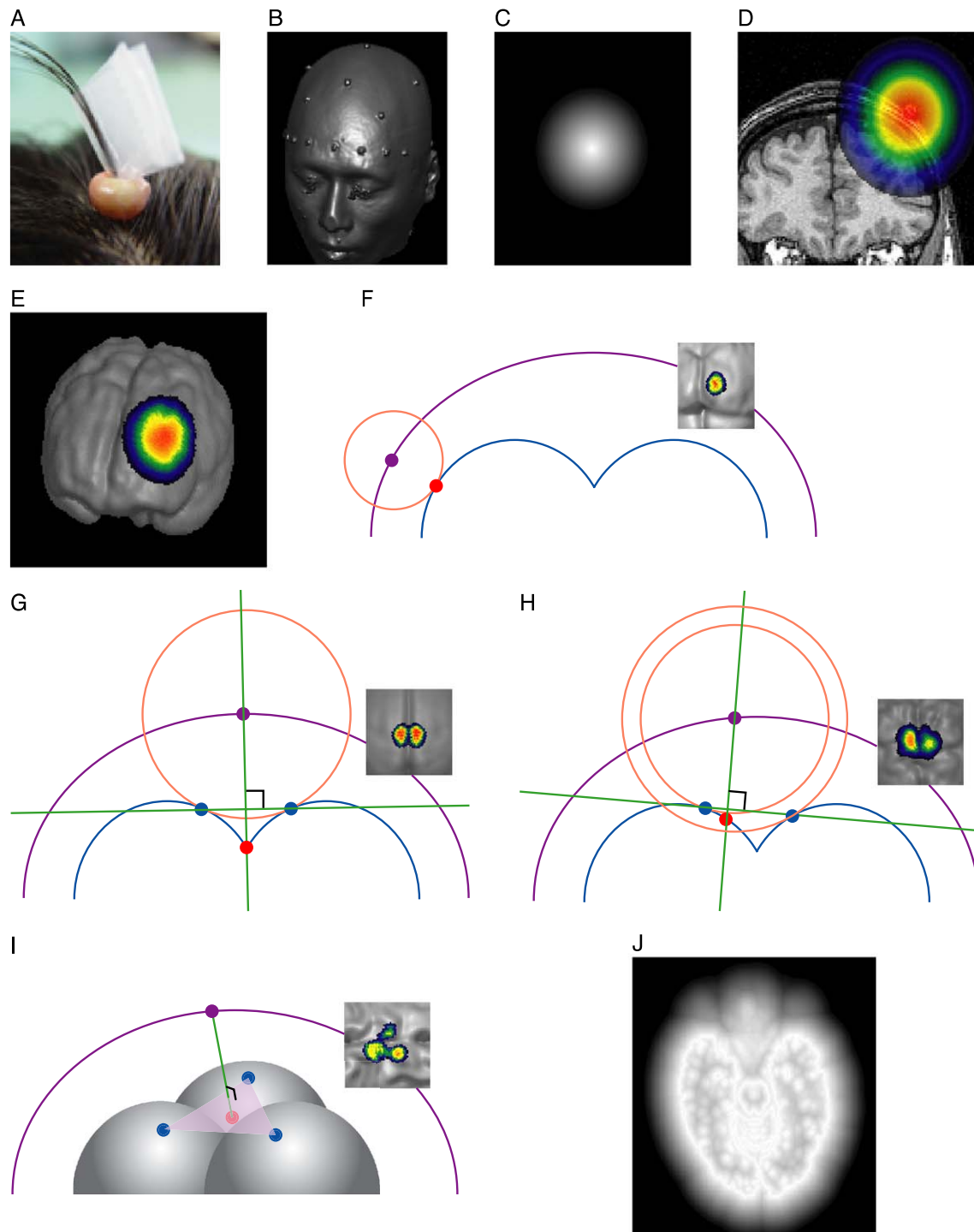
10–20 Marker placement

To reproduce a typical situation in NIRS and TMS experiments in which a fully experienced EEG technologist is usually not available, we selected two operators who were moderately experienced (several dozen times) with marking using the 10–20 system. We instructed them to determine the 10–20 marker locations for each subject according to the international 10–20 system (Fig. 1) (Jasper, 1958). In the original 10–20 system, lateral measurement along the central coronal plane starts at the preauricular points, but due to difficulty in their detection, these points are often replaced with external auditory canals in clinical situations. In addition, this alternative is easier to detect in computerized skin surface images for future automatic 10–20 measurements. Thus, we used the upper limits of the external auditory canals as the starting points for central coronal measurement. The positions included 19 of the 21 standard positions in the 10–20 system, omitting ears. To visualize the standard positions in MRI, we prepared fatty markers made of pine nuts (Fig. 2A) since most commercially available positional markers had yielded little signal and could not be affixed to hairy regions with direct contact to skin. The fatty marker was bead-shaped with a diameter of 7 mm and a tunnel hole with a diameter of 3 mm in the center. We placed the fatty marker in each 10–20 standard position so that the marker and the skin were in direct contact. For bald regions, we fixed the beads with medical tape. For hairy regions, we fixed the beads by threading hairs into the beads and fixed them together with stationary tape (Fig. 2A).

Magnetic resonance imaging

MRI images were acquired using a 1.0-T MR scanner (MAGNEX EPIOS10, Shimadzu, Kyoto, Japan). A T1-weighted, three-dimensional gradient-echo sequence was used to produce 256 continuous axial slices of 1 mm thickness covering the entire cerebrum and the fatty head-surface markers (repetition time = 37 ms, echo time = 10 ms, flip angle 30°, field of view 230 mm × 193 mm, 256 × 214 matrix). The MRI images were stored in the *analyze* format (raw head images).

Table 1
Anatomical locations of international 10–20 cortical projection points

	Labeling by Talairach Daemon				Manual labeling			
	Anatomy	%	BA	%	Anatomy	%	BA	%
Fp1	L FL Superior frontal G	97	10	100	L FL Superior frontal G	94	10	100
	L FL Medial frontal G	2			L FL Middle frontal G	6		
Fp2	R FL Superior frontal G	96	10	100	R FL Middle frontal G	65	10	100
	R FL Middle frontal G	4			R FL Superior frontal G	35		
F3	L FL Superior frontal G	56	10	47	L FL Middle frontal G	81	9	63
	L FL Middle frontal G	44	9	43	L FL Superior frontal G	19	10	31
F4	R FL Middle frontal G	60	10	49	R FL Middle frontal G	98	9	52
	R FL Superior frontal G	40	9	34	R FL Superior frontal G	2	46	25
F7	L FL Inferior frontal G	84	47	81	L FL Inferior frontal G	88	47	63
	L FL Middle frontal G	16	45	13	L FL Middle frontal G	13	45	19
F8	R FL Inferior frontal G	94	47	94	R FL Inferior frontal G	100	47	60
	R FL Middle frontal G	6	45	6			45	29
C3	L PL Postcentral G	77	3	60	L PL Postcentral G	65	3	35
	L FL Precentral G	15	6	15	L FL Precentral G	35	4	29
C4	R PL Postcentral G	89	3	60	R PL Postcentral G	87	3	44
	R FL Precentral G	11	1	17	R FL Precentral G	9	1	24
T3	L TL Middle temporal G	94	21	94	L TL Middle temporal G	88	21	88
	L TL Superior temporal G	6	22	6	L TL Superior temporal G	12	22	12
T4	R TL Middle temporal G	96	21	95	R TL Middle temporal G	85	21	85
	R TL Superior temporal G	4	22	5	R TL Superior temporal G	15	22	15
P3	L PL Superior parietal L	59	7	71	L PL Angular G	89	39	89
	L PL Precuneus	24	19	24	L PL Supramarginal G	10	40	10
P4	R PL Superior parietal L	75	7	82	R PL Angular G	63	39	63
	R PL Precuneus	18	19	18	R OL Superior occipital G	22	19	22
T5	L TL Middle temporal G	61	37	51	L TL Middle temporal G	54	21	49
	L OL Inferior temporal G[a]	15	21	22	L TL Inferior temporal G	31	37	37
T6	R TL Middle temporal G	66	37	54	R TL Middle temporal G	52	21	40
	R OL Middle occipital G	19	39	24	R TL Inferior temporal G	25	37	37
O1	L OL Middle occipital G	69	19	48	L OL Middle occipital G	100	19	53
	L OL Cuneus	13	18	48			18	47
O2	R OL Middle occipital G	68	18	61	R OL Middle occipital G	88	18	71
	R OL Cuneus	20	19	33	R OL Superior occipital G	9	19	26

The two most likely two anatomical structures and Brodmann's area are shown. Note that anatomical structures and Brodmann's areas that are based on histochemical structures do not always coincide. Abbreviations: BA = Brodmann's area, L = left, R = right, FL = frontal lobe, TL = temporal lobe, PL = parietal lobe, OL = occipital lobe, G = gyrus, L = lobule.
[a] The Talairach Daemon program sometimes provides labels with mismatches between the lobe and gyrus.

Table 2
Locations of international 10–20 markers on head surface

	MNI coordinates				Talairach coordinates			
	Position			SD	Position			SD
	x	y	z		x	y	z	
Fp1	− 26.1	83.5	− 0.1	5.9	− 25.9	80.9	− 4.0	7.5
Fp2	32.1	81.3	− 0.2	5.3	31.8	78.8	− 4.0	7.0
Fz	− 0.1	53.3	70.6	10.3	− 0.1	54.9	62.3	9.8
F3	− 42.6	58.0	39.6	11.5	− 42.2	58.0	33.6	11.0
F4	46.9	56.7	40.2	9.5	46.5	56.8	34.2	9.0
F7	− 68.5	37.9	− 5.9	6.6	− 67.8	36.4	− 6.8	7.0
F8	71.4	35.6	− 7.8	6.2	70.7	34.2	− 8.2	6.3
Cz	0.6	− 12.7	101.4	7.5	0.6	− 7.6	93.8	7.3
C3	− 62.7	− 12.7	69.8	9.7	− 62.1	− 9.1	64.7	9.3
C4	64.2	− 15.2	69.9	8.8	63.6	− 11.5	65.0	8.4
T3	− 84.6	− 20.7	− 10.8	8.5	− 83.7	− 20.5	− 8.1	8.0
T4	86.0	− 25.5	− 9.4	7.4	85.1	− 25.1	− 6.7	6.8
Pz	− 0.2	− 76.6	88.5	9.0	− 0.2	− 70.1	85.0	8.7
P3	− 46.8	− 88.2	58.8	10.5	− 46.4	− 82.8	58.3	10.0
P4	44.8	− 87.9	59.6	9.5	44.4	− 82.4	59.1	8.9
T5	− 72.2	− 72.4	0.6	9.3	− 71.5	− 70.1	4.2	10.7
T6	70.8	− 75.6	4.1	8.7	70.1	− 73.1	7.6	10.0
O1	− 31.9	− 112.6	17.3	12.6	− 31.6	− 108.3	21.4	12.6
O2	28.1	− 112.9	19.3	13.5	27.8	− 108.5	23.2	13.3
All				9.2				9.2

All values are in millimeters. SD stands for standard deviation.

Determination of the 10–20 marker positions on head surface

For each subject, we visualized the fatty markers with the head surface (Fig. 2B) by viewing the MRI images using the MRIcro program (Rorden and Brett, 2000) and then determined their coordinates in the following manner. First, we roughly estimated the positions of the markers in three-dimensional coordinates manually, in the three-dimensional rendered image mode. We determined the marker position as the voxel at the center axis of the fatty marker contact head surface. Second, we checked the marker position as viewed in sagittal, coronal, and axial slices in the slice viewer and made fine adjustments. To mark the determined positions digitally, we drew spheres with a radius of 3 mm from the marker coordinates in a separate *analyze* file. For this purpose, we developed a computer program called DrawMSphere that displays the distance from a given voxel coordinate as a gradient and saves it in the *analyze* format (distM image). The program is available upon request. Finally, we overlaid the head surface and the sphere images and re-checked the marker positions in the three-dimensional rendered image mode of MRIcro.

Determining cortical positions underlying the 10–20 markers

For each subject, we segmented the head image into gray matter, white matter, and cerebrospinal fluid using the SPM99 program (Friston et al., 1995). We then extracted the brain from the segmented images and saved them in the *analyze* format (cortical images). To compensate for the extreme convolution of the cortical surface, we smoothed the cortical image using the SPM99 at full width at half-maximum (FWHM) setting at 8 mm. Using the DrawMSphere program, we drew gradient spheres from the 10–20 markers in an *analyze* file (Figs. 2C,D). We overlaid the gradient spheres onto the cortical image using the MRIcro (Fig. 2E). Viewing the overlaid image along the cortical surface generates a contour map showing the distance between the 10–20 markers and their underlying cortical surfaces. From the contour map, we estimated its center, that is, the closest point on the cortex from the corresponding 10–20 marker, as follows. When the center region of the contour map is on a gyrus, the closest point should be found as a single point (Fig. 2F). In this case, we defined the point as a cortical projection point of a 10–20 position. When the center region of the contour map is on a sulcus or fissure, we selected two to four points on the gyri that sandwich or surround the sulcus and represent local minimum distances (Figs. 2G–I). To the line defined by the two minimum-distance points or to the plane defined by the three minimum-distance points, we drew a normal line from the 10–20 marker position (a Matlab tool box for this procedure is available upon request). We defined a cortical projection point as the point at which the normal line intersects the cortical surface (Figs. 2G–I). In some extreme cases where we found four minimum-distance points, we drew two lines defined by two neighboring, non-overlapping points. We next drew normal lines from the 10–20 marker position to the two lines and obtained two separate intersections. By reducing four points to two, we could apply the procedure above. Similarly, we tested the other combination of two lines, and applied the average value of the two combinations.

We checked the cortical projection points using the same procedure as in estimating the coordinates for the 10–20 markers. We calculated the depth of the cortical surface at each 10–20 marker position as the distance between the 10–20 marker and its cortical projection points. For later use, we drew spheres with a radius of 3 mm from the cortical projection points and saved them in an *analyze* format (distCS image).

Table 3
Locations of international 10–20 cortical projection points

	MNI coordinates				Talairach coordinates			
	Position			SD	Position			SD
	x	y	z		x	y	z	
Fp1	− 21.5	70.2	− 0.1	5.0	− 21.3	68.0	− 3.0	7.5
Fp2	28.4	69.1	− 0.4	5.1	28.1	66.9	− 3.6	6.8
Fz	0.6	40.9	53.9	9.8	0.6	42.1	47.5	9.5
F3	− 35.5	49.4	32.4	9.2	− 35.1	49.3	27.4	8.8
F4	40.2	47.6	32.1	8.6	39.8	47.6	27.2	8.2
F7	− 54.8	33.9	− 3.5	6.5	− 54.2	32.7	− 4.4	8.4
F8	56.6	30.8	− 4.1	6.2	56.0	29.7	− 4.7	8.0
Cz	0.8	− 14.7	73.9	8.3	0.8	− 10.8	68.6	8.1
C3	− 52.2	− 16.4	57.8	8.0	− 51.7	− 13.2	53.9	7.7
C4	54.1	− 18.0	57.5	7.1	53.6	− 14.8	53.7	6.8
T3	− 70.2	− 21.3	− 10.7	6.5	− 69.5	− 21.1	− 8.1	7.2
T4	71.9	− 25.2	− 8.2	6.2	71.2	− 24.7	− 5.8	6.4
Pz	0.2	− 62.1	64.5	9.2	0.2	− 57.2	62.3	8.8
P3	− 39.5	− 76.3	47.4	7.4	− 39.1	− 71.7	47.3	7.1
P4	36.8	− 74.9	49.2	7.6	36.5	− 70.3	48.8	7.2
T5	− 61.5	− 65.3	1.1	7.8	− 60.9	− 63.2	3.9	9.2
T6	59.3	− 67.6	3.8	7.3	58.7	− 65.4	6.4	8.0
O1	− 26.8	− 100.2	12.8	10.1	− 26.6	− 96.5	16.1	9.7
O2	24.1	− 100.5	14.1	11.1	23.9	− 96.7	17.3	10.5
All				7.9				8.2

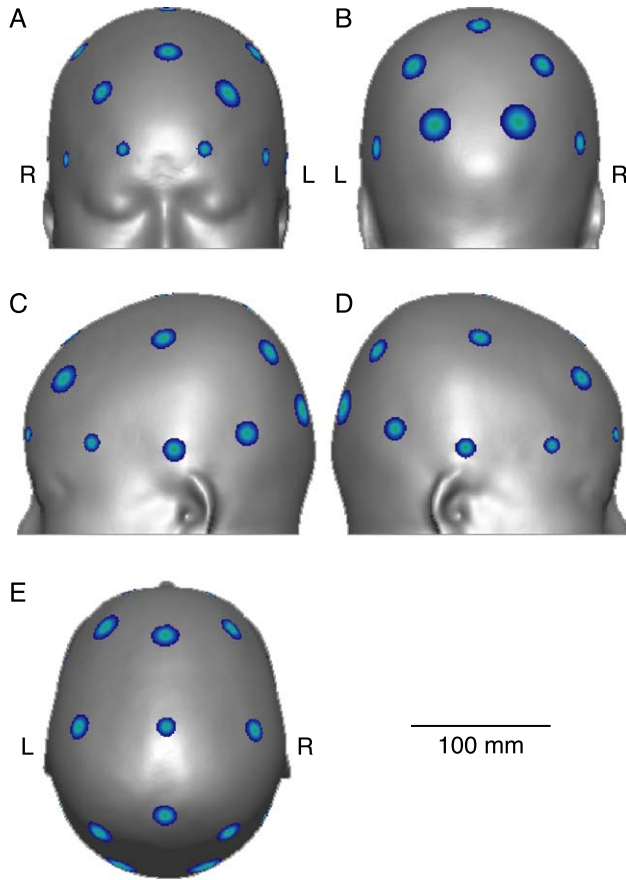All values are in millimeters. SD stands for standard deviation.

Fig. 3. Locations of 10–20 standard positions on a head surface. All positions are overlaid on the averaged head surface image of 17 subjects normalized to the MNI152 standard template (17headAVE). The centers of color gradients represent the locations of the most likely MNI coordinates for the 10–20 standard positions. The edges of color gradients represent the boundaries defined by the standard deviation. Right and left are indicated as R and L when necessary. (A) Frontal view. (B) Occipital view. (C) Left temporal view. (D) Right temporal view. (E) Top view.

distorted by normalization. Across subjects, we calculated the mean coordinate locations

$$(\bar{x}, \bar{y}, \bar{z}) \;=\; \left(\frac{\sum x}{n}, \frac{\sum y}{n}, \frac{\sum z}{n} \right)$$

and standard deviations

$$\text{SD} \;=\; \sqrt{\frac{\sum(x - \bar{x})^2 \;+\; \sum(y - \bar{y})^2 \;+\; \sum(z - \bar{z})^2}{n - 1}}$$

(or estimation for the root of the variance, σ_r) for the 10–20 markers and their cortical projection points. We next prepared a head image by averaging the normalized head images of the 17 subjects (17headAVE image) and overlaid the 10–20 markers on 17headAVE image. We also prepared a brain image by extracting the brain from the normalized head image of each subject and averaged the images across subjects (17brainAVE image). We overlaid the 10–20 cortical projection points on the
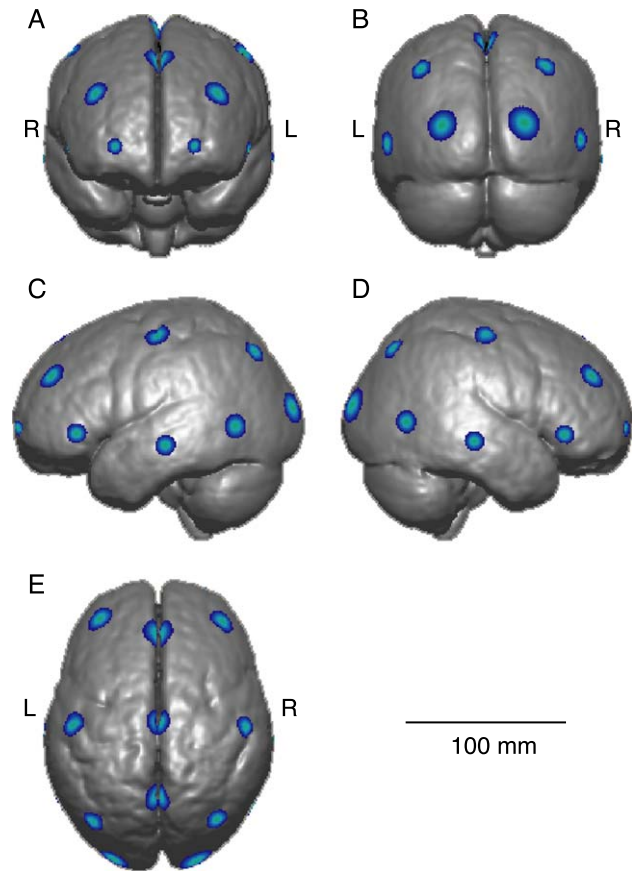

Fig. 4. Locations of 10–20 cortical projection points on a brain surface. All positions are overlaid on the averaged brain image of 17 subjects normalized to the MNI152 standard template (17brainAVE). The centers of color gradients represent the locations of the most likely MNI coordinates for the 10–20 cortical projection points. The edges of color gradients represent the boundaries defined by the standard deviation. Right and left are indicated as R and L when necessary. (A) Frontal view. (B) Occipital view. (C) Left temporal view. (D) Right temporal view. (E) Top view.

Normalization of the marker and cortical projection points and inter-subject integration

Using SPM99, we normalized raw head images of each subject to the standard MNI152 template (T1.img template in SPM99) (Brett et al., 2002; Friston et al., 1995). The template is also known as ICBM152, the standard template of the International Consortium for Brain Mapping (ICBM, http://www.loni.ucla.edu/ICBM/). We set all parameters to default settings except for an interpolation method. The default setting (bilinear) of the interpolation method was recommended for fMRI images resliced at the realignment stage. Since our data were structural MRI images without realignment, we used the "sinc interpolation" setting recommended for non-realigned MRI images. For each subject, we also transformed the distM and distCS images using the same algorithm employed to normalize the raw head images (NdistM and NdistCS images). The resultant images display the 10–20 marker positions and their cortical projection points in the standard MNI coordinates. We read the coordinate positions of the voxel that is located at the center of gravity of each sphere, which has been slightly

17brainAVE image. We used DrawMSpheres to visualize the locations of the markers and their projections with standard deviations (Figs. 3 and 4). We also converted the 10–20 markers and their cortical projection points from MNI coordinates to Talairach coordinates according to the following equations (http://www.mrc-cbu.cam.ac.uk/Imaging/mnispace.html):

$$\text{for } z_m \geq 0, (x_t, y_t, z_t) = (0.9900x_m, 0.9688y_m + 0.0460z_m,$$
$$-0.0485y_m + 0.9189z_m),$$
$$\text{for } z_m < 0, (x_t, y_t, z_t) = (0.9900x_m, 0.9688y_m + 0.0420z_m,$$
$$-0.0485y_m + 0.8390z_m),$$

where (x_m, y_m, z_m) are the given MNI coordinates and (x_t, y_t, z_t) are the Talairach coordinates to be obtained. For the coordinate positions in Talairach space, we labeled the 10–20 cortical projection points anatomically using the Talairach Daemon pro-

gram (Lancaster et al., 2000) for each subject. The Talairach Daemon program scans probable anatomical locations from a given position in the Talairach space. When a single anatomical place was found, we selected it to represent the anatomical place for the 10–20 cortical projection point of the subject (e.g., F3 of the subject A was 100% on the middle frontal gyrus). When two or more anatomical places were found in border regions, we used probabilistic constituents of each anatomical place (e.g., the probability of F3 of subject B was 60% in the middle and 40% in the inferior frontal gyri). By integrating probabilistic constituents among all the subjects, we determined probabilistic anatomical places for each of the 10–20 cortical projection points (Table 1). We also examined anatomical structures for the 10–20 cortical projection points of each subject manually using not-normalized cortical images in reference to anatomical atlases (Mai et al., 1997; Ono et al., 1990; Talairach and Tournoux, 1988; Neuronames,
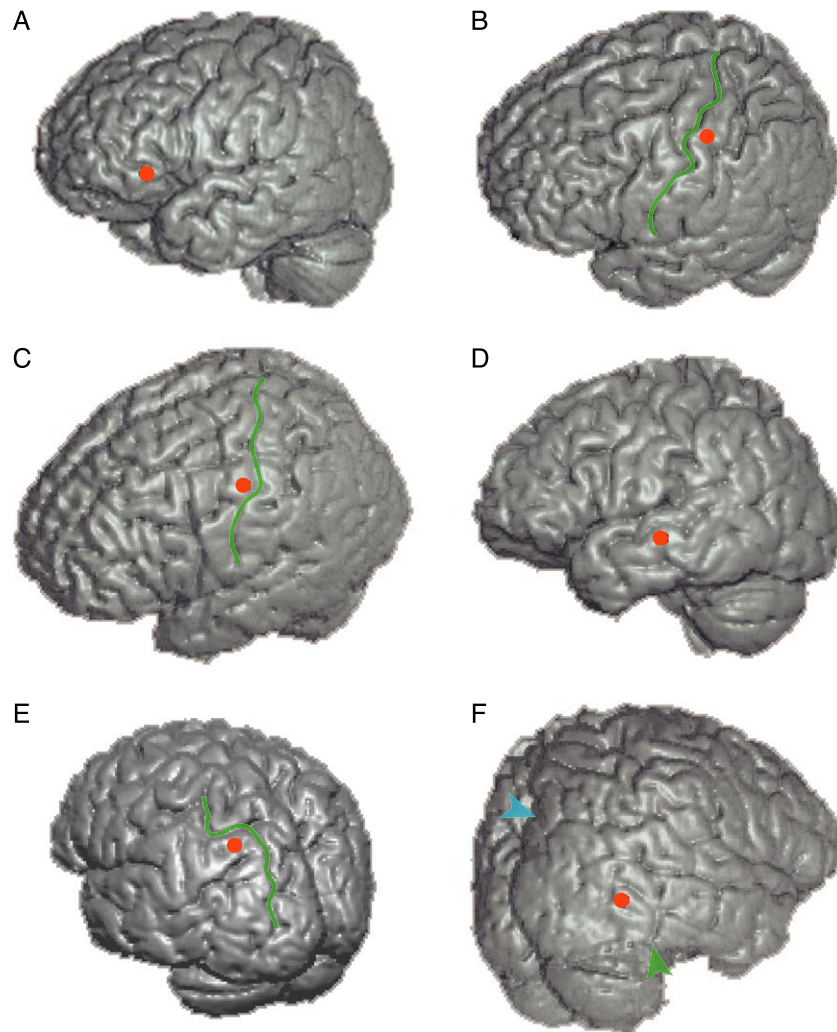

Fig. 5. Examples of anatomical locations of cortical projection points. Some specific anatomical cases in selected subjects are shown for descriptive purposes. (A) F7 (red circle) on the frontal lobe. Left temporal view is shown. (B) C3 (red circle) on the postcentral gyrus of the parietal lobe. Left temporal view is shown. The central fissure is superimposed as a green line. (C) C3 (red circle) on the precentral gyrus of the frontal lobe. Left temporal view is shown. The central fissure is superimposed as a green line. (D) T3 (red circle) on the temporal lobe. Left temporal view is shown. (E) P3 (red circle) on the angular gyrus. Left temporal view is shown. The intraparietal sulcus is superimposed as a green line. (F) T6 (red circle) on the border between the temporal and the occipital lobes. Right temporal view is shown. The preoccipital notch is superimposed as a green arrowhead. The parieto-occipital sulcus is superimposed as a blue arrowhead.
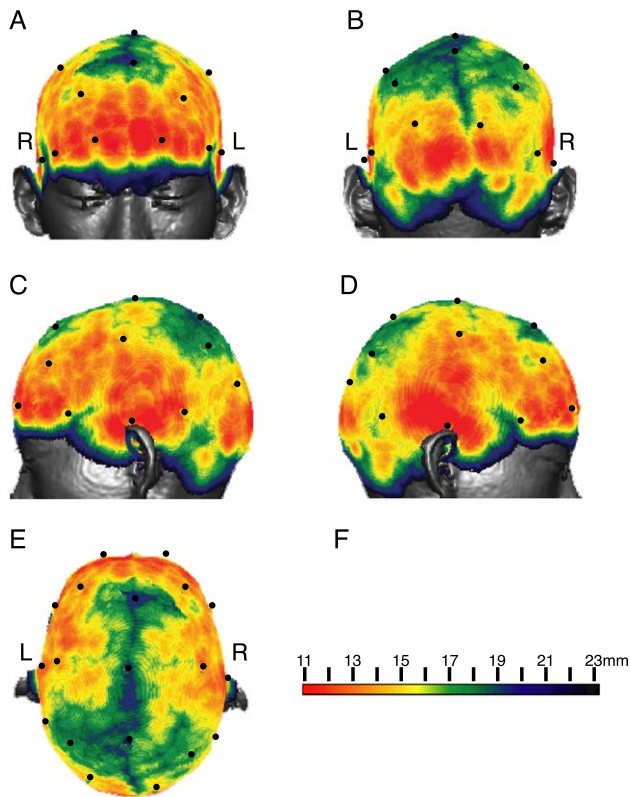
Fig. 6. Cortical surface depth map for one subject. The cortical depth distribution is exhibited on the head surface of a subject before normalization. The locations of the 10–20 standard positions are indicated as dots. Right and left are indicated as R and L when necessary. (A) Frontal view. (B) Occipital view. (C) Left temporal view. (D) Right temporal view. (E) Top view. (F) Color gradient bar indicating cortical depth.

(http://rprcsgi.rprc.washington.edu/neuronames/index.html). A 10–20 cortical projection point represented as a sphere with a 3-mm radius was divided into three or four fractions of equal sizes. As in the case of labeling with the Talairach Daemon, we determined probabilistic constituents of each anatomical place in units of fractions of the 3-mm-radius sphere, and integrated all probabilistic constituents among all the subjects.

Cortical surface depth map

From the cortical image of each subject, we extracted the cortical surface alone using the ExtSurf program developed for this purpose. ExtSurf extracts the outer edge of a cortical image and saves it in the *analyze* format (available upon request). We next prepared a color gradient map showing distances from the extracted cortical surface. For this purpose, we developed a computer program, DrawMap, which sequentially draws circles with a gradient from each voxel of a given cortical surface and saves the image in the *analyze* format (available upon request). This program starts by drawing a gradient circle at an arbitrary voxel of the cortical surface. It next draws another gradient circle from a neighboring voxel. For voxels where two gradient circles overlap, the program assigns only the stronger signal to the voxel. In this way, the program scans across the cortical surface and generates a distance distribution from the cortical surface,

expressed as a gradient (BSurf image) (Fig. 2J). Overlaying the BSurf image on the head image using the MRIcro program generates a cortical surface depth map showing the distance distribution from the cortical surface (Fig. 6).

For inter-subject integration, we transformed a BSurf image of a subject using the same algorithm that had been applied for normalizing the raw head image to the standard MNI template (NBSurf image). Using the Mean function of SPM99, we averaged the NBSurf images of all the subjects. We overlaid the averaged NBSurf image on the 17headAVE image using the MRIcro program. This yielded the averaged cortical surface depth map showing the mean distance distribution from the cortical surface among all the subjects (Fig. 7).

Results

The stereotactic coordinates of the locations of the 10–20 standard positions on the head surface and their cortical projection points based on the 17 subjects expressed in MNI and Talairach spaces are presented in Tables 2 and 3. The locations of the 10–20 standard positions on the head surface overlaid on the normalized and averaged head surface of 17 subjects (17headAVE) are depicted in Fig. 3. Fig. 4 illustrates the locations of cortical
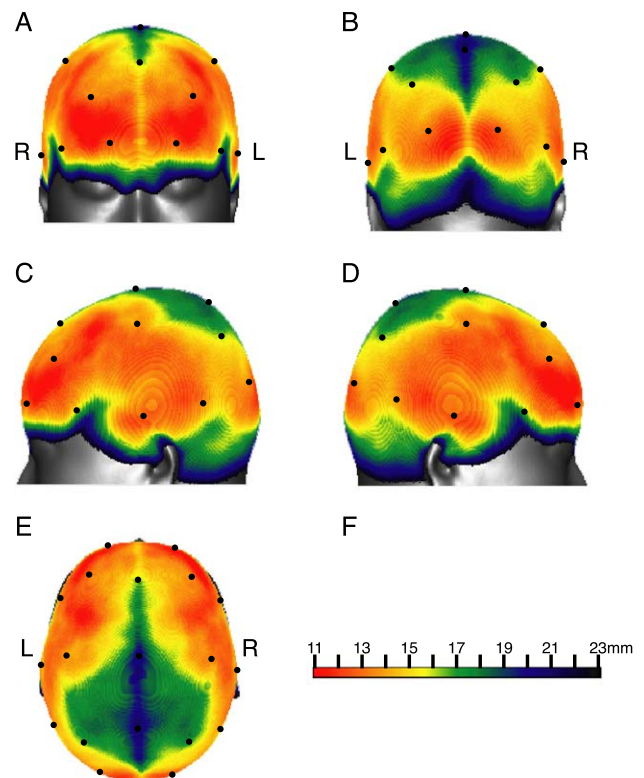

Fig. 7. Cortical surface depth map after intersubject integration. Cortical depth distribution is exhibited on the averaged head surface image of 17 subjects normalized to the MNI152 standard template (17headAVE). The locations of the 10–20 standard positions are indicated as dots. Right and left are indicated as R and L when necessary. (A) Frontal view. (B) Occipital view. (C) Left temporal view. (D) Right temporal view. (E) Top view. (F) Color gradient bar indicating cortical depth.

projection points of 10–20 standard positions overlaid on the averaged brain surface of 17 subjects normalized to MNI space (17brainAVE).

Among the 10–20 standard positions, the locations of Fp1 and Fp2 were the most stable and had the smallest standard deviation in the MNI space. In contrast, the locations of their occipital mirror positions, O1 and O2, varied greatly. Comparing the F7–F8 and T5–T6 pairs, the posterior positions also had larger spatial variations. However, comparing the F3–F4 and P3–P4 pairs, the anterior positions exhibited greater standard deviation.

The relationship between the 10–20 standard positions and their underlying cortical structure is summarized in Table 1, and the following descriptions are based on manual labeling. For descriptions of specific cases, some anatomical examples in selected subjects are shown in Fig. 5. Fp1 and Fp2 are projected either onto the superior or middle frontal gyri, BA10. F7 and F8, which seem to be on the border between the frontal and temporal lobes, are always projected onto the frontal lobe (Fig. 5A). F3 and F4 were either on the superior or middle frontal gyri. C3 and C4 were primarily located behind the central fissure on the postcentral gyrus (Fig. 5B), but in some subjects they were located on the precentral gyrus (Fig. 5C). O1 and O2 were usually on the middle occipital gyrus. T3 and T4 were projected predominantly onto the middle temporal gyrus, BA21 (Fig. 5D). P3 and P4 were usually on the angular gyrus (Fig. 5E). T5 and T6, which seemed to be on the border of occipital and temporal lobes, are more often projected on the temporal lobe, but these were on the border between the occipital and the temporal lobes in one third of the subjects (Fig. 5F). Three midline standard positions, Fz, Cz, and Pz, were located on or near the interhemispheral fissure.

Furthermore, we measured the depth to the cortical surface from all points on the head surface and created an individual cortical surface depth map for each subject (Fig. 6) and a composite cortical surface depth map for all subjects (Fig. 7). Note that this map describes the gross distribution of cortical surface depth along the scalp; sulci and fissures are filled in due to the algorithm used. Considering finer structural features, we also examined the cortical surface depth measured as the distance between the 10–20 standard positions on the head surface and their cortical projection points (Table 4). From the frontal polar region where the cortex is located most shallowly, the shallow area extends superio-postaly, detours from the silvian fissure to the temporal side, and further extends to the occipital polar region. In contrast, the parietal regions are located deeper, especially along the intra-hemispherical fissure. Near the silvian fissure, the cortex was deeper. In contrast, the central fissure did not affect the cortical depth.

Discussion

The ultimate goal of our research is to present a three-dimensional anatomical platform that enables intra- and intermodal comparison of transcranial brain imaging data. As the first step, we examined the cranio-cerebral correlation and probabilistically expressed the locations of 10–20 standard positions and their cortical projection points in the standard stereotactic coordinates for brain-imaging studies with anatomical considerations. We also examined the depth of the cortical surface from the skin along the head surface and expressed its distribution in a cortical surface depth map. In this discussion, we will examine the validity of the method and consider how our findings are applicable to actual NIRS and TMS studies. We will then propose solutions for comparing intermodal data.

Cerebro-cranial correlation

The essence of our study lies in expressing the 10–20 standard positions and their cortical projection points in standard coordinates. Conceptually, our approach is an extension of that of Homan et al. (1987), where they projected the 10–20 standard positions onto the Brodmann's atlas (Brodmann, 1909, 1912) and thus expressed their cortical projection points in two-dimensional Brodmann coordinates. Now that Brodmann's two-dimensional atlas has been expanded to the three-dimensional Talairach atlas (Talairach and Tournoux, 1988), we projected the 10–20 standard positions onto three-dimensional space.

We used a rather unique projection method. We basically defined the cortical projection point of a 10–20 standard position as the closest point on the cortical surface to the 10–20 standard position. An exception to the rule was when a 10–20 standard position was located over a sulcus or fissure; in that case, we estimated the cortical projection points based on the closest points on the banks of the neighboring gyri. This projection method differs from that used by Homan et al. (1987), where they projected the 10–20 standard positions perpendicularly to the sagittal plane of the Brodmann's atlas. Their method intrinsically suffers from a problem associated with projecting a space on a plane. While central areas (e.g., around C3) are well projected, the marginal areas (e.g., around Cz) are extremely skewed and compressed into a small area. Towle et al. (1993) and Lagerlund et al. (1993) circumvented the cortical projection problem by fitting the scalp onto a sphere. Their methods greatly reduced skew but still yielded minor shape problems because the scalp is not spherical but rather similar to an ellipsoidal body with some gentle cavities. Thus, some points (e.g., F8 and F4) could not be projected well on the cortical surface by the spherical fitting method. This is a merit, not a problem, for EEG studies where the source is estimated for the whole brain. In NIRS, however, the near-infrared light beamed from a light source onto the head surface travels laterally through tissue owing to scattering among tissues and reaches the detector in a separate position on the head surface, so that the source is estimated only on the lateral cortical surface in NIRS. Similarly, the magnetic field applied by TMS is

Table 4

Depths from head to cortical surfaces at international 10–20 positions

	Mean	SD		Mean	SD		Mean	SD
Fp1	13.5	2.2	Cz	25.8	4.0	P4	17.6	2.2
Fp2	12.6	1.9	C3	16.0	2.3	T5	12.7	1.9
Fz	19.7	2.4	C4	15.6	1.9	T6	13.0	1.4
F3	13.8	1.8	T3	12.9	2.1	O1	13.8	1.5
F4	13.9	1.9	T4	13.1	2.1	O2	13.7	1.2
F7	14.5	2.4	Pz	25.9	4.2			
F8	16.7	3.1	P3	16.9	2.6	All	15.9	5.6

All values are in millimeters. SD stands for standard deviation. Cortical depth is defined as the distance between a given 10–20 standard position on the head surface and its cortical projection point. The row indicated as "all" shows the mean cortical depth for all the 10–20 standard positions in 17 subjects and their standard deviations.

effective only within 4 cm of the head surface. In this sense, our projection method is optimal for these transcranial studies. For future distribution of our method, we are now developing an algorithm to enable automatic data processing.

Normalization to the standard brain facilitates expression of the 10–20 cortical projection points in the Talairach coordinates (Brett et al., 2002), which enables anatomical labeling with user-friendly computer programs such as the Talairach Daemon (Lancaster et al., 2000). However, individual variations in the anatomical locations of the gyrus and sulcus remain in the Talairach space, even after normalization to the standard template. Thus, estimating anatomical locations from a given Talairach coordinate can result in mislocations. As shown in Table 1, our anatomical predictions and those of the Talairach Daemon were fairly consistent, but we sometimes found obvious discrepancies. For example, the Talairach Daemon program predicted that most P3 and P4 cortical projection points were located on the superior parietal lobule, but we found that some of them were on the angular gyrus (Fig. 5E). For this reason, manual labeling determined visually is still necessary in anatomical analyses. Thus, we based the following anatomical discussion on manual anatomical labeling.

The locations of the 10–20 standard positions measured in this study roughly corresponded to those obtained in former studies. Among the 10–20 standard positions, the most controversial are the C3–C4 pairs, which Jasper (1958) marked on the postcentral region in a figure and mentioned as precentral in the text. Homan et al. (1987) proposed that the C3–C4 pairs are located predominantly on the precentral gyrus. In contrast, the following study by Steinmetz et al. (1989) suggested that C3 and C4 were located either on the postcentral or precentral cortices, depending on individual anatomy. Towle et al. (1993) also reported that C3 and C4 were overlaid either on the postcentral or precentral cortices. Our study also supports individual variation. However, there was postcentral bias in contrast to the predominant locations proposed by Homan et al. (1987). Our selection of external auditory canals instead of periauricular points as the starting points for central coronal measurement can cause postcentral bias of a few millimeters, but this is not sufficient to explain our observation. The most plausible reason for such discrepancy is that subjects of different races were used in the two studies. All the subjects in our study were Mongoloids while Homan et al. (1987) probably used primarily Caucasian subjects, although a clear description was not found. Mongoloids generally have flatter occiputs than Caucasoids. We expect a flatter occiput yields a more forward relative brain position or more backward relative scalp position. This may enable cranial C3 and C4 positions to shift backward, producing the postcentral bias observed in the current study. Thus, we suggest that C3 and C4 can overlay either on the precentral or postcentral gyri, and that racial as well as individual factors should be considered.

Consistent with former studies (Homan et al., 1987; Towle et al., 1993), we found F7 and F8 exclusively overlaid on the frontal lobe, not on the temporal lobe, even though they were near the sylvian fissure.

Homan et al. (1987) stated the other controversial points, T5 and T6, were on temporal lobes. However, our study demonstrated that they were either on the temporal or occipital lobes, depending on the individual. Since the border of the temporal and occipital lobes itself is unclear, it would be more appropriate to allow individual variations rather than to specify the exact anatomical location.

Among the 10–20 standard positions, O1 and O2 exhibited the greatest individual variation, and the locations of posterior standard positions tended to be less reliable. However, this tendency was not apparent in the study of Lagerlund et al. (1993). This discrepancy may be due to different fitting methods used in the two studies. Lagerlund et al. (1993) used the spherical fitting method, which does not involve deformation, while our method employs normalization to a standard template. Variations in the shape of the posterior skull and difficulty in locating the inion have been indicated in previous studies (Steinmetz et al., 1989; Towle et al., 1993), and our method is also sensitive to these variations.

In contrast, our study as well as that of Lagerlund et al. (1993) revealed less reliability of F3, F4, P3, and P4 than the other 10–20 standard positions. Because these points are the last to be placed and their placement depends on other standard positions, their positions tend to vary.

In the current study, we succeeded in probabilistically expressing the anatomical structures of the cortical projection points for the 10–20 standard positions. Such a probabilistic approach should be valuable for handling the variables of individual cortical anatomy.

Consideration on error components

We examined distributions of the 10–20 standard positions on the head surface and their cortical projections in MNI space and determined the center coordinates for the distributions (Tables 2 and 3). In principle, the center coordinates represent the expected locations of these positions on the canonical head and brain in MNI space. We also expressed the breadths of the distributions as standard deviations. Assuming that the distributions are Gaussian in 3D, 61% of the observations will be less than the standard deviation away from the mean coordinate position (see Appendix A for detailed calculations). These statistical treatments will enable researchers to estimate the location on the cortical surface corresponding to a particular 10–20 position with a known error.

The standard deviations presented in Tables 2 and 3 include mainly three error factors in their combined forms. The first is the error in head-surface measurement using the 10–20 system. Towle et al. (1993) reported that the mean displacement of the 10–20 standard positions was 1.4 mm in three measurements done on the same day and 2.5 mm among three measurements on different days. Slightly greater standard deviations will be obtained. It is theoretically possible to reduce such human errors by hard training, but in the current study, we have chosen to allow such errors and incorporate them in the estimation.

The second error factor results from the individual differences in the gross structures of the brain and scalp. To express heads and brains of different sizes in the same coordinates, they should be fit, or normalized, to standard template brain and head images in each coordinate system. Since normalization is imperfect, a normalized brain does not match the template used and therefore does not match the canonical brain. This disparity is the third error component. Choice of different templates, coordinate systems, or normalization programs will result in different error values.

For single-channel NIRS and TMS, expected values provided in Tables 2 and 3 can be used directly. However, the other error factors, namely, the disparity caused by a fixed inter-optode distance in multichannel NIRS and the various sizes of human heads, should be considered for multichannel NIRS. Examination

on such error factors needs further study. We are currently investigating positional and structural estimations for various multichannel NIRS optode settings.

Cortical depth information

The depth of the cortical surface from the head surface is an important factor to be considered in NIRS measurement. The best detector–illuminator separation for a cortical surface as a function of depth from the head surface is yet to be theoretically addressed, primarily because studies on near-infrared light propagation using a head model or computer simulation have been performed on a head of a fixed size. Based on research using a head model or computer simulation, the following general rule applies. A longer inter-optode distance enables measuring deeper cortical activity according to the simple diffusion model (Feng et al., 1993; Tsunazawa et al., 1994). Too small an inter-optode distance, such as 15 mm, does not allow near-infrared light to access the gray matter (Okada et al., 1997). The partial mean optical path length (that indicates a path length of near-infrared light that travels through tissue per unit distance) remains relatively constant for inter-optode distances exceeding 25 mm. However, a 10-mm increase of inter-optode distance above 20 mm results in a 90% reduction of the optical signal (Farrell et al., 1992; Okada et al., 1997). Thus, with the above in mind, NIRS researchers have to empirically determine the optimum inter-optode distance depending on the region to be examined. A cortical surface depth map that exhibits a global distribution of the cortical surface depth along the head surface can be of great value for this process (Fig. 7).

In addition, we examined intersubject and interchannel variances of cortical depth, which raises another important issue in multichannel NIRS measurement that has not been discussed. That is, these variations cause differences in effective optical pathlengths among subjects and channels. In usual NIRS measurements where the inter-optode difference is fixed, the optical path length also seems to be fixed, but this is only so for cortical contributions to the optical path length. The scalp, which has as low permeability as cortical gray matter, exhibits variance among subjects and channels, which further results in different optical path lengths. This difference produces rather complicated effects in actual NIRS measurement. Since NIRS utilizes changes of signal intensity and not the signal intensity itself, its estimation of Hb concentration change is considered relatively robust compared to differences in signal intensity caused by different optical path lengths (Gratton et al., 2001). Nevertheless, the relative Hb concentration change measured by NIRS is still sensitive to differences in optical path length. Our data showed that the depth of the cortical surface from the skin had a standard deviation of 2.3 mm. This means the optical path length differs among individuals by 5 mm or so for a round-trip of the signal in the depth direction even though the inter-optode distance is fixed. An increase in the optical path length affects Hb concentration by producing a higher degree of error because the lower signal intensity results in a lower signal-to-noise ratio. Thus, NIRS measurement of the deeper cortex results in greater variance of Hb concentration. Different cortical depths among channels can cause a similar problem of varying optical path lengths when a large area is measured by multichannel NIRS. The issues discussed above need to be considered when performing detailed quantitative analysis on cortical activation by NIRS.

In TMS, the magnetic field and resultant electric field attenuate as functions of distance, and human tissue has little effect on it. For example, when a double coil is used, a 5-mm increase in depth reduces the electric field roughly 30% (Jalinous, 1991). Thus, brain depth information is useful for determining a suitable power and compensating regional differences in the effective electric field.

Toward intermodal data comparison

In this study, we presented three essential steps for intermodal data comparison. The first is the conversion of the 10–20 standard positions by projecting them onto the cortical surface as their cortical projection points. The second is the probabilistic expression of these cortical projection points in the standard MNI and Talairach brains. The third is the probabilistic anatomical description of these cortical projection points. Thus, via guidance from the international 10–20 system, we can now compare the data obtained from transcranial brain-mapping modalities with those from others. This may be sufficient for literature reading by experienced researchers, but does not allow the inexperienced to intuitively grasp different brain-mapping data. Thus, the intermodal data comparison should be more automated. Ideally, NIRS and TMS mapping data may be displayed on the standard MNI brain by setting locations of the reference and some of the channels relative to the 10–20 standard positions. Transcranial brain-mapping data can then be easily integrated into the functional probabilistic atlas proposed by ICBM (Mazziotta et al., 2000). The development of such an algorithm should be explored in the future.

To expand the data sets and improve the method, we have prepared our data in a relatively extensible way; namely, all the data are presented in the MNI and Talairach coordinates. Racial differences in brain structure have been reported (Zilles et al., 2001), so one limitation of our initial data set is that it was based only on Mongoloid subjects. To compensate for racial differences and to achieve more pan-human representation, data sets for Negroid or Caucasoid samples should be included in the current format. Moreover, the cortical projection points for the international 10–10 or extended 10–20 system can be exhibited in the same format. We believe that such expandability will enable our initial data sets to be developed into a form of database that can further links to the intermodal brain-imaging database. Update of our initial data set and related data are available at our web site (http://brain.job.affrc.go.jp/).

Acknowledgments

Appendix A

We consider the case where the three-dimensional point set has a normal distribution. We define $f(p)$ as the probability for

which each point $p(x, y, z)$ is realized. We put $r^2 := x^2 + y^2 + z^2$. Without loss of generality, we can set,

$$f(p) = e^{-(x^2 + y^2 + z^2)} = e^{-r^2}.$$

By using the following equation

$$\left\{\int_{-\infty}^{\infty} f(p)\mathrm{d}p\right\}^3 = \int_{-\infty}^{\infty}\int_{-\infty}^{\infty}\int_{-\infty}^{\infty} e^{-(x^2 + y^2 + z^2)}\mathrm{d}x\mathrm{d}y\mathrm{d}z$$

$$= \int_0^{\infty}\int_0^{2\pi}\int_0^{\pi} e^{-r^2}r^2\sin\theta\mathrm{d}\theta\mathrm{d}\varphi\mathrm{d}r$$

$$= 4\pi\int_0^{\infty} e^{-r^2}r^2\mathrm{d}r = \pi^{\frac{3}{2}},$$

we have the expectation of r^2, $\langle r^2 \rangle$.

$$\langle r^2 \rangle = \left\{4\pi\int_0^{\infty} r^2(e^{-r^2}r^2)\mathrm{d}r\right\} \div \left(4\pi\int_0^{\infty} e^{-r^2}r^2\mathrm{d}r\right) = \frac{3}{2}.$$

We put $R_1 := \sqrt{\langle r^2 \rangle} = \sqrt{\frac{3}{2}}$. Similarly, we can obtain the expectation of r, $\langle r \rangle$.

$$R_2 := \langle r \rangle = \left\{4\pi\int_0^{\infty} r(e^{-r^2}r^2)\mathrm{d}r\right\}$$
$$\div \left(4\pi\int_0^{\infty} e^{-r^2}r^2\mathrm{d}r\right) = \frac{2}{\sqrt{\pi}}.$$

For a real number R, the probability $\mathrm{Prob}(R)$ of the point p such that $x^2 + y^2 + z^2 \leq R$ is given by the following equation:

$$\mathrm{Prob}(R) = \left(\int_0^{R} e^{-r^2}r^2\mathrm{d}r\right) \div \left(\int_0^{\infty} e^{-r^2}r^2\mathrm{d}r\right)$$

$$= \mathrm{Erf}(R) - \frac{2R}{\sqrt{\pi}}e^{-R^2},$$

where $\mathrm{Erf}(R) = \frac{2}{\sqrt{\pi}}\int_0^{R} e^{-r^2}\mathrm{d}r$.

If $R = R_1$, then we have $\mathrm{Prob}(R_1) = 0.61$. Thus, if the estimation of R_1 is given as a standard deviation, 61% of the points of the 3D Gaussian distribution should be less than the standard deviation away from the mean.

Some previous research used mean displacement, and thus we describe its statistical use. If $R = R_2$, then we have $\mathrm{Prob}(R_2) = 0.53$. Thus, if the estimation of R_2 is given as a mean displacement, or the mean of the absolute distance of each point from the center of the distribution, 53% of the points should be less than the mean displacement away from the mean.

Similarly, we have calculated the following values for convenience, $\mathrm{Prob}(1.45R_1) = 0.90$, $\mathrm{Prob}(1.63R_1) = 0.95$, and $\mathrm{Prob}(2R_1) = 0.99$. Thus, 90%, 95%, and 99% of the points are approximately less than 1.45, 1.63, and 2 standard deviations away from the mean.

References

Barker, A.T., Jalinous, R., Freeston, I.L., 1985. Non-invasive magnetic stimulation of human motor cortex. Lancet 1 (8437), 1106–1107.

Blume, W.T., Buza, R.C., Okazaki, H., 1974. Anatomic correlates of the ten–twenty electrode placement system in infants. Electroencephalogr. Clin. Neurophysiol. 36, 303–307.

Brett, M., Johnsrude, I.S., Owen, A.M., 2002. The problem of functional localization in the human brain. Nat. Rev. Neurosci. 3, 243–249.

Brodmann, K., 1909. Vergleichende Lokalisationslehre der Grosshirnrinde in ihren Prinzipien dargestellt auf Grund des Zellenbaues. J.A. Barth, Leipzig (In German).

Brodmann, K., 1912. Neue Ergebnisse über die vergleichende histologische Lokalisation der Grosshirnrinde. Anat. Anz. 41, 157–216 (In German).

Curra, A., Modugno, N., Inghilleri, M., Manfredi, M., Hallett, M., Berardelli, A., 2002. Transcranial magnetic stimulation techniques in clinical investigation. Neurology 59, 1851–1859.

Farrell, T.J., Patterson, M.S., Wilson, B., 1992. A diffusion theory model of spatially resolved, steady-state diffuse reflectance for the noninvasive determination of tissue optical properties in vivo. Med. Phys. 19, 879–888.

Feng, S., Zeng, F., Chance, B., 1993. Monte Carlo simulations of photon migration path distributions in multiple scattering media. SPIE (Photon migration and imaging in random media and tissues) 1888, 88.

Friston, K.J., Ashburner, J., Frith, C.D., Poline, J.B., Heather, J.D., Frackowiak, R.S.J., 1995. Spatial registration and normalization of images. Hum. Brain Mapp. 2, 165–189.

Gevins, A.S., Illes, J., 1991. Neurocognitive networks of the human brain. Ann. N.Y. Acad. Sci. 620, 22–44.

Gratton, G., Goodman-Wood, M.R., Fabiani, M., 2001. Comparison of neuronal and hemodynamic measures of the brain response to visual stimulation: an optical imaging study. Hum. Brain Mapp. 13, 13–25.

Homan, R.W., Herman, J., Purdy, P., 1987. Cerebral location of international 10–20 system electrode placement. Electroencephalogr. Clin. Neurophysiol. 66, 376–382.

Hoshi, Y., Oda, I., Wada, Y., Ito, Y., Yamashita, Y., Oda, M., Ohta, K., Yamada, Y., Tamura, M., 2000. Visuospatial imagery is a fruitful strategy for the digit span backward task: a study with near-infrared optical tomography. Brain Res. Cogn. Brain Res. 9, 339–342.

Isobe, K., Kusaka, T., Nagano, K., Okubo, K., Yasuda, S., Kondo, M., Itoh, S., Onishi, S., 2001. Functional imaging of the brain in sedated newborn infants using near infrared topography during passive knee movement. Neurosci. Lett. 299, 221–224.

Jack, C.R., Marsh, W.R., Hirschorn, K.A., Shabrough, F.W., Cascino, G.D., Karwoski, R.A., Robb, R.A., 1990. EEG scalp electrode projection onto 3-dimensional surface rendered images of the brain. Radiology 176, 413–418.

Jalinous, R., 1991. Technical and practical aspects of magnetic nerve stimulation. J. Clin. Neurophysiol. 8, 10–25.

Jasper, H.H., 1958. The ten–twenty electrode system of the International Federation. Electroencephalogr. Clin. Neurophysiol. 10, 367–380.

Lagerlund, T.D., Sharbrough, F.W., Jack Jr., C.R., Erickson, B.J., Strelow, D.C., Cicora, K.M., Busacker, N.E., 1993. Determination of 10–20 system electrode locations using magnetic resonance image scanning with markers. Electroencephalogr. Clin. Neurophysiol. 86, 7–14.

Lancaster, J.L., Woldorff, M.G., Parsons, L.M., Liotti, M., Freitas, C.S., Rainey, L., Kochunov, P.V., Nickerson, D., Mikiten, S.A., Fox, P.T., 2000. Automated Talairach Atlas labels for functional brain mapping. Hum. Brain Mapp. 10, 120–131.

Mai, J.K., Assheuer, J., Paxinos, G., 1997. Atlas of the Human Brain. Academic Press, San Diego.

Mazziotta, J.C., Toga, A.W., Evans, A.C., Fox, P., Lancaster, J., Woods, R., 2000. A probabilistic approach for mapping the human brain. In: Toga, A.W., Mazziotta, J.C. (Eds.), Brain Mapping: The Systems. Academic Press, San Diego, pp. 141–156.

Miyai, I., Tanabe, H.C., Sase, I., Eda, H., Oda, I., Konishi, I., Tsunazawa, Y., Suzuki, T., Yanagida, T., Kubota, K., 2001. Cortical mapping of gait in humans: a near-infrared spectroscopic topography study. NeuroImage 14, 1186–1192.

Morris, H.H., Lüders, H., Lesser, R.P., Dinner, D.S., Klem, G.H., 1986. The value of closely spaced scalp electrodes in the localization of epileptiform foci: a study of 26 patients with complex partial seizures. Electroencephalogr. Clin. Neurophysiol. 63, 107–111.

Myslobodsky, M.S., Bar-Ziv, J., 1989. Locations of occipital EEG electrodes verified by computed tomography. Electroencephalogr. Clin. Neurophysiol. 72, 362–366.

Myslobodsky, M.S., Coppola, T., Bar-Ziv, J., Weinberger, D.R., 1990. Adequacy of the international 10–20 electrode system for computed neurophysiologic topography. J. Clin. Neurophysiol. 7, 507–518.

Okada, E., Firbank, M., Schweiger, M., Arridge, S.R., Cope, M., Delpy, D.T., 1997. Theoretical and experimental investigation of near-infrared light propagation in a model of the adult head. Appl. Opt. 36, 21–31.

Ono, M., Kubik, S., Abernathey, C.D., 1990. Atlas of the Cerebral Sulci. Thieme, New York.

Rorden, C., Brett, M., 2000. Stereotaxic display of brain lesions. Behav. Neurol. 12, 191–200.

Steinmetz, H., Furst, G., Meyer, B.U., 1989. Craniocerebral topography within the international 10–20 system. Electroencephalogr. Clin. Neurophysiol. 72, 499–506.

Takahashi, K., Ogata, S., Atsumi, Y., Yamamoto, R., Shiotsuka, S., Maki, A., Yamashita, Y., Yamamoto, T., Koizumi, H., Hirasawa, H., Igawa, M., 2000. Activation of the visual cortex imaged by 24-channel near-infrared spectroscopy. J. Biomed. Opt. 5, 93–96.

Talairach, J., Tournoux, P., 1988. Co-planar Stereotaxic Atlas of the Human Brain. Thieme, New York.

Terao, Y., Ugawa, Y., 2002. Basic mechanisms of TMS. J. Clin. Neurophysiol. 19, 322–343.

Towle, V.L., Bolanos, J., Suarez, D., Tan, K., Grzeszczuk, R., Levin, D.N., Cakmur, R., Frank, S.A., Spire, J.P., 1993. The spatial location of EEG electrodes: locating the best-fitting sphere relative to cortical anatomy. Electroencephalogr. Clin. Neurophysiol. 86, 1–6.

Tsunazawa, Y., Eda, H., Takada, M., 1994. Analytical formula describing the effect of deep optical absorber in multiple scattering media. In: Ohzu, H., Komatsu, S. (Eds.), Optical Methods in Biomedical and Environmental Sciences. Elsevier Sciences, Amsterdam, pp. 35–38.

Van den Elsen, P.A., Viergever, M.A., 1991. Marker guided registration of electromagnetic dipole data with tomographic images. In: Colchester, A.C., Hawkes, D.J. (Eds.), Information Processing in Medical Imaging. Springer, Berlin, pp. 142–154.

Villringer, A., Chance, B., 1997. Non-invasive optical spectroscopy and imaging of human brain function. Trends Neurosci. 20, 435–442.

Villringer, A., Dirnagl, U., 1995. Coupling of brain activity and cerebral blood flow: basis of functional neuroimaging. Cerebrovasc. Brain Metab. Rev. 7, 240–276.

Watanabe, E., Yamashita, Y., Maki, A., Ito, Y., Koizumi, H., 1996. Non-invasive functional mapping with multi-channel near infra-red spectroscopic topography in humans. Neurosci. Lett. 205, 41–44.

Watanabe, E., Maki, A., Kawaguchi, F., Takashiro, K., Yamashita, Y., Koizumi, H., Mayanagi, Y., 1998. Non-invasive assessment of language dominance with near-infrared spectroscopic mapping. Neurosci. Lett. 256, 49–52.

Zilles, K., Kawashima, R., Dabringhaus, A., Fukuda, H., Schormann, T., 2001. Hemispheric shape of European and Japanese brains: 3-D MRI analysis of intersubject variability, ethnical, and gender differences. NeuroImage 13, 262–271.